



# Modeling of concentration polarization and permeate flux variation in a roto-dynamic reverse osmosis filtration system



Anoop Jogdand, Abhijit Chaudhuri \*

Department of Applied Mechanics, Indian Institute of Technology Madras, Chennai 600036, Tamil Nadu, India

## HIGHLIGHTS

- CFD model to predict concentration polarization (CP) on membrane interface
- Roto-dynamic filtration system used for reverse osmosis in laminar regime of operation
- Shear rate created by rotor, helps to reduce CP layer and enhance the permeate flux.
- Permeate flux does not change much with aspect ratio but increases with feed pressure.
- Feed flow rate increase shear rate but not effective to increase permeate flux.

## ARTICLE INFO

### Article history:

Received 26 November 2014

Received in revised form 10 July 2015

Accepted 11 July 2015

Available online 7 August 2015

### Keywords:

Roto-dynamic filtration

Reverse osmosis

Concentration polarization

Shear rate

Feed flow

CFD

## ABSTRACT

Concentration polarization (CP) is a critical issue during desalination by cross-flow reverse osmosis (CFRO) filtration system and it is known that shear rate on the membrane surface can help its mitigation. Roto-dynamic filtration systems provide an easy way to generate high shear rate on membrane surface, and hence reducing CP. However the studies related to the growth of CP layer in roto-dynamic CFRO filtration is very limited. In this paper we developed a computational frame-work where flow and solute transport were simulated using ANSYS-Fluent V14.5 but physics of reverse osmosis through the membrane were implemented using “user defined functions” (UDFs). The development of the CP layer in a roto-dynamic CFRO filtration system has been discussed for different operating conditions such as inlet location, rotation speed, gap between the disk and the membrane and feed pressure. The effects of these parameters on permeate flux are also discussed. It is noted that angular speed of rotor and feed pressure are very effective parameters than others to enhance the permeate discharge. The understanding about the CP layer growth and its influence on permeate flux from the present study will help in better and efficient design of roto-dynamic CFRO filtration systems.

© 2015 Elsevier B.V. All rights reserved.

## 1. Introduction

Researches in desalination and wastewater recycling are presently directed towards enhancing the filtration efficiency and reducing the cost and environmental footprint of these processes [1]. Spiral wound membrane is an important component of cross flow reverse osmosis (CFRO) systems as employed during desalination and wastewater recycling. These membranes face major operational issues such as scaling and fouling, which further lead to uneven flow distribution and increase in friction. Accumulation of salt on the membrane surface or concentration polarization (CP) is identified as the main cause, which further reduces the permeate flux due to osmotic pressure build-up across the membrane. CP in spiral wound systems has been extensively

studied numerically and experimentally [2–13]. One of the widely used mitigation measure includes the use of spacers, facilitating the flow on the retentate side to increase of the shear rate on the membrane surface. The effect of shear rate cannot be totally harnessed in spiral wound cross low filtration systems as there is a trade-off between the reduction of CP layer and the increase in pressure drop [1]. Jaffrin [14,15] discussed the role of roto-dynamic filtration systems, which involve a rotating disc over a membrane, or a rotating membrane in an enclosed chamber. This rotary action imparts motion to the feed flow and generates high shear rate on the membrane surface. Thus roto-dynamic filtration systems are promising as they inherently decouple the pressure drop and shear rate on the membrane surface. The benefits of dynamic filtration are two folds [16]. Firstly these ensure lesser accumulation of solute on the membrane surface and hence decrease the solute/salt transmission to the permeate side. Secondly, the rotating disk systems within a certain range of angular velocity produce different flow

\* Corresponding author.

E-mail address: [abhijit.chaudhuri@iitm.ac.in](mailto:abhijit.chaudhuri@iitm.ac.in) (A. Chaudhuri).

structures with co-existence of circular and spiral waveforms. These waveforms, which are formed on both rotating and stationary walls [24] assist further reduction of CP layer on the stationary membrane.

The CP layer formation, its growth and its behavior with varying flow characteristics has been extensively studied for CFRO systems. The growth of the CP layer along the flow has been observed experimentally and successfully replicated numerically with the help of CFD calculations. The two way coupling between the permeate flux which builds the CP layer and the CP layer in-turn reducing the flow to the membrane through resistance is established and can be simulated. It is also known that the effect of increase in shear rate on the membrane surface reduces solute concentration polarization and hence the osmotic pressure [36,37]. This in turn increases the trans-membrane driving pressure and hence the permeate flux rate. Also it is known that the CP layer keeps on growing along the length of the channel [35–37].

Unfortunately in the literature, there is a dearth of studies which try to build a similar understanding for CP in roto-dynamic systems. This essentially forms a motivating factor for the authors to work towards fundamental understanding of the concentration polarization in dynamic filtration systems. To the best of authors' knowledge, the past attempts and studies [28–30,38] related to dynamic filtration mainly focused on experimental studies of ultra and nano-filtration processes. Some of those also performed computational simulations to compare the integral permeate flux with the experimental results. It was apparent from those studies that operating parameters such as angular speed of the rotating plate ( $\Omega$ ), gap between the plate and membrane ( $h$ ) and magnitude of the feed flow ( $Q$ ) affect permeate flux. However there are no discussions available in literature about the effect of above-mentioned parameters on the development of the CP-layer, in time and space inside a dynamic filtration system. It is important to quantify the effect of these parameters on the shear rate, CP layer thickness and permeate flux. So this gap in literature defines a goal of this study. It will help to develop an understanding and hence the suitable range of these parameters to build efficient and economic roto-dynamic filtration systems. However there are certain issues such as the requirement of huge surface areas and operational cost for large-scale RO or NF plant, may be of concern for its suitability in commercial desalination plant. So further researches may be needed to design suitable roto-dynamic RO filtration systems, which can overcome the above-mentioned limitations.

The analysis of roto-dynamic filtration systems will have two major aspects, one being the hydrodynamics of such systems and second being the solute transport modeling for the RO process. The permeate flow rates through the membrane in such filtration systems are usually very small as compared to the feed flow rates. Hence it can be assumed that the effect of permeate flow rate on the flow pattern within the rotary reverse osmosis system is negligible and flow can be analyzed based on the extensive studies of closed stator–rotor cavity systems in fluid mechanics literatures. For the stator–rotor cavity system, the disk rotation leads to an axisymmetric flow pattern with two distinct boundary layers formed near the stator and the rotor [17]. In addition to the swirl velocity, the flow within the boundary layers near rotor and stator is radially outward and inward respectively [18]. Thus a flow field resembling the cross flow filtration over the membrane is developed. These boundary layers may be merged or disjoint. In the case of a disjoint boundary layer a centrally rotating or non-rotating fluid core exists [17,19]. The nature of flow field inside a roto-dynamic system is governed by the angular speed of the rotor and the gap between stator and rotor [20–24]. The dimensionless parameters, which can be used to characterize various base flow patterns in a stator–rotor cavity, are Reynolds number ( $Re$ ) and aspect ratio ( $G$ ) [25]. In terms of the velocity scale ( $\Omega R$ ) and length scales ( $R, h$ ) these parameters are defined as follows,

$$Re = \frac{\Omega R^2}{\nu} \text{ and } G = \frac{h}{R}, \quad (1)$$

where  $\Omega, R, h$  and  $\nu$  are respectively angular speed of the rotor, radius of the rotary system, gap between rotor and stator, and kinematic viscosity of fluid. Daily et al. [25] presented a figure indicating different flow regimes in the ( $Re, G$ ) parameter space. This figure serves as the essential reference map distinguishing various flow regimes such as laminar, turbulent, joint or disjoint boundary layers etc. For continuous operation of cross-flow filtration, a feed flow ( $Q$ ) is maintained by including inlet and outlet to the rotor cavity system. Poncet et al. [26,27] demonstrated that the magnitude of the feed flow affects the nature of the base flow created due to rotation of the rotor. They proposed the following dimensionless variable to quantify the effect of feed flow rate on the velocity field.

$$Q^* = \frac{Q}{\nu R} \quad (2)$$

They found experimentally that weak through-flow preserves the base flow inherent to a stator–rotor cavity system, but as the feed flow becomes strong it dominates the flow field characteristics and the flow pattern can significantly change. Bouzerar et al. [28] studied dynamic-ultra and nano filtration systems. They compared the vibratory separation systems with the rotary systems. They found that the rotary systems were superior in performance. Torras et al. [29,30] performed experimental study on ultra and nano-filtration rotary disk device. They observed the increase in the trans-membrane pressure due to the decrease in osmotic pressure, which was an outcome of a reduced CP layer. Thus their experimental investigation confirmed the influence of shear rate on permeate flux. Later Ling et al. [31] performed numerical studies considering the permeate flux along with fluid flow, but neglecting the species transport. They discussed the radial variation of permeate flux, trans-membrane pressures and effect of spacers.

Accurate prediction of concentration polarization during cross-flow filtration in a rotary system requires a suitable model for physics of reverse osmosis. Wijmans et al. [32] provided the basic review on the pore flow model and the solution–diffusion RO model. They derived the required phenomenological equations based on the solution–diffusion model and validity of the model was demonstrated. Sabalani et al. [33] critically reviewed the published studies on CP in ultrafiltration and reverse osmosis processes and suggested quantification techniques with a review of experiments performed to visualize and quantify concentration polarization. Paul [34] presented the reformulation of the solution diffusion theory so as to bring the non-linear flux behavior in to picture which becomes significant with increased feed flow concentrations. The solution diffusion model seems to be the widely accepted one and many researchers used this approach to simulate the fully coupled fluid flow, species transport and reverse osmosis. Ahmad et al. [35] simulated CP layer development in channel along the direction of flow. They used ANSYS-Fluent V6.0 to model flow and transport but assumed the membrane to be impermeable wall while simulating the fluid flow inside the channel. Wardeh et al. [36] simulated flow and transport in a channel that was filled with spacer using CFX for reverse electro-dialysis applications. For incorporating the RO physics, both of these numerical studies developed user defined functions, which were linked to the solver. Recently Diaz et al. [37] performed an experimental study and simulated using COMSOL for modeling RO in a slit type channel. The effect of cross flow and shear rate on the concentration polarization was studied at different Reynolds numbers in the laminar regime. These researches helped understand the growth of the CP layer in the cross flow reverse osmosis process.

In the present work we have simulated RO filtration in a roto-dynamic system using ANSYS-Fluent V14.5. We have noted that in most of the reported work in the literature [28–30], the values of  $Q^*$  were quite high (approximately between 230 and 691), and the effect of disk rotation was superseded by the feed flow rate to a large extent. In those previous studies the shear rate on the membrane surface was mainly generated due to the feed flow rate and the disk rotation seemed to be redundant. This important aspect was considered in this paper

during investigating the effects of various parameters on concentration polarization. In this paper we also have explained the salt accumulation patterns as a function of flow configuration and operating variables. The values of Reynolds number and aspect ratios have been chosen as proposed by Daily et al. [25] (see Fig. 2 in [23]) to ascertain laminar flow. This can be considered as a new contribution to the existing knowledge in developing industrial reverse osmosis systems.

## 2. Mathematical modeling of roto-dynamic RO system

In this study the dynamic reverse osmosis filtration system considered comprises of a disk of radius 'R' and a membrane. The disk rotates with an angular speed of ' $\Omega$ ' and is placed at a distance 'h' above the membrane. For continuous operation of the cross-flow filtration system, a constant feed flow of amount Q, is imposed through the inlet and outlet location as shown in Fig. 1a. The size of the inlet and outlet are taken such that the width of the inlet/outlet along the radial direction is 5% of the radius R of the disk. However the locations of inlet and outlet can be interchanged to create opposite feed flow configurations. Fig. 1a and b represent the outward flow configuration where the inlet and outlet are located near the axis and edge of the disk respectively.

### 2.1. Governing equations

The modeling of permeate flux through the membrane involves solving for fluid flow along with solute transport within the rotor-cavity system and through thin porous layer representing the membrane. In a stator-rotor cavity system the geometry, boundary conditions and fluid properties are constant in tangential direction. Hence the three-dimensional flow and transport processes can adequately be modeled as an axisymmetric problem. The axisymmetric continuity and momentum balance equations in cylindrical coordinates ( $r, \theta$  &  $z$ ) are given below.

$$\frac{\partial \rho}{\partial t} + \frac{1}{r} \frac{\partial (\rho r v_r)}{\partial r} + \frac{\partial (\rho v_z)}{\partial z} = 0 \quad (3)$$

$$\rho \left( \frac{\partial v_r}{\partial t} + v_r \frac{\partial v_r}{\partial r} - \frac{v_\theta^2}{r} + v_z \frac{\partial v_z}{\partial z} \right) = - \frac{\partial p}{\partial r} + \frac{4}{3} \frac{\partial}{\partial r} \left( \mu \frac{\partial}{\partial r} (r v_r) \right) - \frac{2}{3} \frac{\partial}{\partial r} \left( \mu \frac{\partial v_z}{\partial z} \right) + \frac{\partial}{\partial z} \left( \mu \frac{\partial v_r}{\partial r} \right) + \frac{\partial}{\partial z} \left( \mu \frac{\partial v_z}{\partial z} \right) \quad (4)$$

$$\rho \left( \frac{\partial v_z}{\partial t} + v_r \frac{\partial v_z}{\partial r} + v_z \frac{\partial v_z}{\partial z} \right) = - \frac{\partial p}{\partial z} + \frac{1}{r} \frac{\partial}{\partial r} \left( \mu r \frac{\partial v_z}{\partial r} \right) + \frac{1}{r} \frac{\partial}{\partial r} \left( \mu \frac{\partial v_r}{\partial z} (r v_r) \right) - \frac{2}{3r} \frac{\partial}{\partial z} \left( \mu \frac{\partial}{\partial r} (r v_r) \right) + \frac{4}{3} \frac{\partial}{\partial z} \left( \mu \frac{\partial v_z}{\partial z} \right) \quad (5)$$

$$\rho \left( \frac{\partial v_\theta}{\partial t} + v_r \frac{\partial v_\theta}{\partial r} + v_z \frac{\partial v_\theta}{\partial z} + \frac{v_r v_\theta}{r} \right) = \frac{1}{r^2} \frac{\partial}{\partial r} \left( \mu r^3 \frac{\partial}{\partial r} \left( \frac{v_\theta}{r} \right) \right) + \frac{\partial}{\partial z} \left( \mu \frac{\partial v_\theta}{\partial z} \right) \quad (6)$$

Here  $v_r$ ,  $v_z$  and  $v_\theta$  are respectively radial, axial and swirl velocity components. Fluid pressure, density and viscosity are denoted as  $p$ ,  $\rho$ , and  $\mu$  respectively. The axisymmetric species transport equation is given as,

$$\frac{\partial (\rho C)}{\partial t} + \frac{1}{r} \frac{\partial (\rho r v_r C)}{\partial r} + \frac{\partial (\rho v_z C)}{\partial z} = \frac{1}{r} \frac{\partial}{\partial r} \left( r D \frac{\partial C}{\partial r} \right) + \frac{\partial}{\partial z} \left( D \frac{\partial C}{\partial z} \right) \quad (7)$$

where  $C$  and  $D$  are respectively solute concentration and diffusivity of the solute. Here the flow was considered to be in laminar regime. For solute transport, the solution was considered as a binary mixture of water and salt (sodium sulfate). Sodium sulfate was chosen as the salt while simulating concentration polarization because the experimental results were available for sodium sulfate to validate the numerical results. With the change in the type of salt, the osmotic pressure will change and hence the permeate flux. But the accumulation pattern over the membrane surface is governed by the shear rate and fluid circulation above the membrane but not the type of salt. We have accounted for the variations of viscosity, diffusivity, density of the solution with solute concentration. The fluid and transport properties can vary both spatially and temporarily. The following are the relevant relations as taken from [13,37] for modeling concentration dependent fluid and transport properties:

$$D = 1.16 \times 10^{-9} - 3.9 \times 10^{-12} C \quad (8)$$

$$\rho = 0.909C + 997.1 \quad (9)$$

$$\mu = 8.9 \times 10^{-4} + 3.133 \times 10^{-6} C. \quad (10)$$

In the above empirical relations, units for  $C$ ,  $D$ ,  $\rho$ , and  $\mu$  are in g/kg,  $\text{m}^2/\text{s}$ ,  $\text{kg}/\text{m}^3$ , and  $\text{Pa}\cdot\text{s}$  respectively.

### 2.2. Boundary conditions

Along the surfaces of the rotating disk, stationary walls and membranes, no slip conditions for velocities were considered. The stationary sidewall and rotor are impermeable while the permeate flux through the membrane was used to specify the axial velocity component along the membrane. To implement these boundary conditions and further to mimic the rotation of the rotor at a constant angular velocity of  $\Omega$ , the radial, tangential and axial velocities were prescribed as follows:

$$v_\theta = r\Omega, v_r = 0; v_z = 0; \quad @z = h, R_1 \leq r \leq R_2, \forall \theta, \quad (11)$$

where  $R_1$  and  $R_2$  represent the dimensions of the inlet and outlet as shown in Fig. 1b. At the feed inlet the total mass flow rate of water

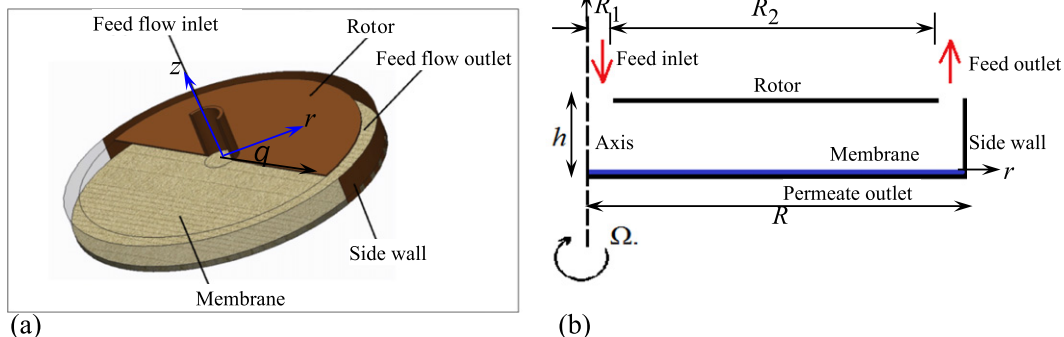


Fig. 1. Schematic diagram of a rotary reverse osmosis filtration system, (a) three dimensional view and (b) axisymmetric representation of the domain.

( $\dot{m} = \text{constant}$ ) was specified while at the outlet the pressure ( $P_{\text{out}} = \text{constant}$ ) was specified.

$$2\pi \int_{R_2}^R v_z \rho r dr = \dot{m}, \quad @z = h \quad (12)$$

$$P = P_{\text{feed}}, \quad @z = h, 0 \leq r \leq R_1, \forall \theta \quad (13)$$

The inlet concentration was also specified as  $C = C_{in}$ . Along the side-wall and surface of membrane (i.e) the flow and transport boundary conditions are given below:

$$v_\theta = 0, v_r = 0, v_z = -J; \quad @z = 0, \forall r, \forall \theta \quad (14)$$

$$v_\theta = 0, v_r = 0, v_z = 0; \quad @r = R, \forall z, \forall \theta. \quad (15)$$

Here  $J$  is the permeate flux (m/s) through the membrane. It is positive as permeate flows downward while leaving through the membrane at  $z = 0$ . The procedure of calculating  $J$  is discussed later. For solute transport, the diffusive solute flux was set to zero along the impermeable boundaries (rotor and side walls) and outlet. This is mathematically represented as,

$$\frac{\partial C}{\partial n} = 0. \quad (16)$$

Here  $n$  corresponds to the coordinate that is the normal to the surface along the impermeable boundaries and outlet. At the membrane interface, the boundary condition for species transport was derived from an appropriate mathematical model for the CFRO process. The mathematical model was based on one dimensional convection–diffusion equation (Eq. (17)) and was coupled with the osmotic pressure law for the permeate flux calculation (Eq. (19)).

$$JC_m + D \left. \frac{\partial C}{\partial z} \right|_m = JC_p, \quad (17)$$

where  $J$  and  $D$  are respectively permeate flux and molecular diffusion. Here the subscripts 'm' and 'p' are used to distinguish the variables at the membrane surface and permeate side. The concentration of salt in permeate side ( $C_p$ ) should be ideally zero, but it was experimentally observed to be a very small fraction of salt concentration,  $C_m$ , at membrane surface. These two are quantified using the rejection coefficient ' $R_c$ ' [37], which is expressed as follows,

$$R_c = 1 - \frac{C_p}{C_m}. \quad (18)$$

Rejection rate is a membrane specific property and its value ranges between 0.95 and 0.98. The expression for permeate flux ( $J$ ) is given below.

$$J = K(\Delta p - \Delta \Pi), \quad (19)$$

where  $K$ ,  $\Pi$  and  $p$  are respectively the membrane constant ( $1.1467 \times 10^{-11}$  m/Pa-s), the osmotic pressure and the fluid pressure. Here  $\Delta$  represents the difference between the values at the membrane surface and permeate side. The osmotic pressure is proportional to concentration. It is determined using the following relation [37]:

$$\Pi = 0.523C. \quad (20)$$

In the above empirical formula the units for,  $C$  and  $\Pi$  are g/kg, and bar respectively.

### 3. Numerical modeling and validation

To simulate cross flow reverse osmosis (CFRO) filtration in a roto-dynamic system using ANSYS-Fluent V14.5 several user defined functions (UDFs) were built to include the physics of reverse osmosis through the membrane. In ANSYS-Fluent, finite volume method was used to solve the governing equations for flow and solute transport. The transport equations were solved in a segregated fashion with SIMPLER (Semi Implicit Pressure Linked Equations, Consistent) pressure velocity coupling. Second order accurate discretization scheme was used for spatial discretization of momentum and solute transport equations. The pressure correction equation was discretized using PRESTO (Pressure Staggering Option) scheme.

Due to absence of any previous results in literature for CFRO filtration in roto-dynamic system, we have performed CFRO simulations for a channel feed flow system and compared our numerical results with the experimental results of Diaz et al. [37]. This serves the purpose of validating our numerical model, which was then used to predict the CP layer in roto-dynamic filtration systems. Diaz et al. [37] showed the concentration polarization on the membrane surface and the resulting reductions in permeate flux. Fig. 2 shows schematic diagram of the computational domain and indicates the boundary conditions for a CFRO system. The governing equations and boundary conditions for channel flow are given below:

$$\frac{\partial \rho}{\partial t} + \frac{\partial(\rho v_x)}{\partial x} + \frac{\partial(\rho v_z)}{\partial z} = 0 \quad (21)$$

$$\frac{\partial(\rho v_x)}{\partial t} + v_x \frac{\partial(\rho v_x)}{\partial x} + v_z \frac{\partial(\rho v_x)}{\partial z} = -\frac{\partial p}{\partial x} + \frac{\partial}{\partial x} \left( \mu \frac{\partial v_x}{\partial x} \right) + \frac{\partial}{\partial z} \left( \mu \frac{\partial v_x}{\partial z} \right) \quad (22)$$

$$\frac{\partial(\rho v_z)}{\partial t} + v_x \frac{\partial(\rho v_z)}{\partial x} + v_z \frac{\partial(\rho v_z)}{\partial z} = -\frac{\partial p}{\partial z} + \frac{\partial}{\partial x} \left( \mu \frac{\partial v_z}{\partial x} \right) + \frac{\partial}{\partial z} \left( \mu \frac{\partial v_z}{\partial z} \right) \quad (23)$$

$$\left( \frac{\partial(\rho C)}{\partial t} + v_x \frac{\partial(\rho C)}{\partial x} + v_z \frac{\partial(\rho C)}{\partial z} \right) = \frac{\partial}{\partial x} \left( D \frac{\partial C}{\partial x} \right) + \frac{\partial}{\partial z} \left( D \frac{\partial C}{\partial z} \right). \quad (24)$$

The boundary conditions for the domain were set as follows. At inlet, constant values were specified for velocity components as well as solute concentration. At the channel outlet for modeling fluid flow the pressure was specified while the solute concentration gradients along  $x$  direction were set to zero at outlet. At the top wall, which is impermeable, a no slip condition for velocity and zero diffusive flux condition for the solute were provided.

$$v_x = V, v_z = 0, C = C_{in}; \quad @x = 0, \forall z \quad (25)$$

$$p = p_{atm}, \frac{\partial C}{\partial x} = 0, \quad @x = L, \forall z \quad (26)$$

$$v_x = 0, v_z = 0, \frac{\partial C}{\partial z} = 0, \quad @z = h, \forall x \quad (27)$$

The boundary conditions along the porous membrane were same as Eqs. (14), (17) and (19).

For numerical modeling of Robin type of boundary condition (Eq. (17)) for species transport at the membrane surface, a separate UDF was written. The discretization scheme and method of inclusion into the solver are discussed below. Porous membrane was modeled as a thin porous medium of thickness  $h_m$ . Since the membrane

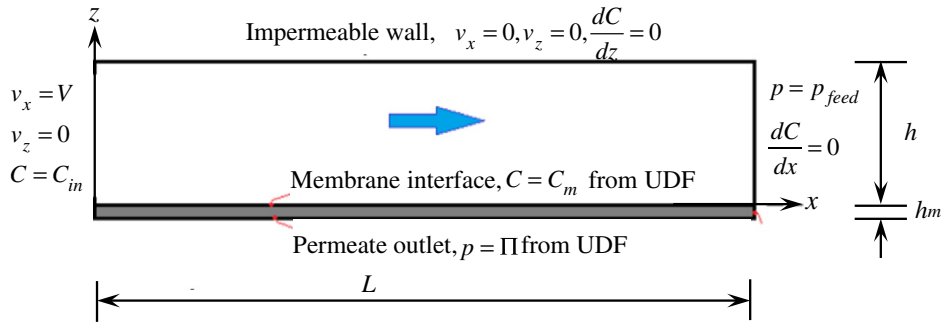


Fig. 2. Schematic diagram of a channel reverse osmosis filtration system.

thickness is very small, following 1-D Darcy equation was solved to calculate the permeate flux ( $J$ ) through the membrane:

$$J = -\frac{k}{\mu} \frac{dp}{dz}. \quad (28)$$

Here  $k$  is the permeability of porous medium. We considered atmospheric fluid pressure at the permeate outlet side of the membrane. We assume that the fluid pressure and concentration of salt reaches equilibrium very fast inside thin porous membrane and the permeate chamber. So there is no need to simulate flow and transport in the permeate chamber. After calculating the value of  $J$  from Eq. (17), it is set as the boundary condition in Eq. (14). Since permeate flux also depends on the osmotic pressure difference, for easiness to implement Eq. (19) in numerical simulation, we considered the pressure at the permeate side ( $p_p$ ) as,

$$p_p = p_{atm} + \Delta\Pi. \quad (29)$$

Here  $\Delta\Pi$  is determined from the values of  $C_m$  and  $C_p$ .

To compare the results and check the accuracy, the concentration gradient term in Eq. (17) was discretized using both first and second order scheme. The expressions of first order accurate and second order accurate backward differences are given below:

$$\left. \frac{\partial C}{\partial z} \right|_m = \frac{C_m - C_A}{\Delta z} + O(\Delta z) \quad (30)$$

$$\left. \frac{\partial C}{\partial z} \right|_m = \frac{-3C_m + 4C_A - C_B}{2\Delta z} + O(\Delta z^2) \quad (31)$$

where  $C_m$ ,  $C_A$ ,  $C_B$  are respectively the concentration at the membrane interface and at adjacent grid points as illustrated in Fig. 3. Here  $\Delta z$  is the spacing between these grid points above the membrane along  $z$  direction. Fig. 3c represents the enlarged view of the computational mesh near the porous membrane. In order to access values of concentration at the nearby cells from the solver, an explicit cell zone was created over the porous zone (RO zone). This zone was just one finite volume cell thick. Based on the number of cell centered values required by the expression (30 or 31), two more explicit fluid zones of one finite volume

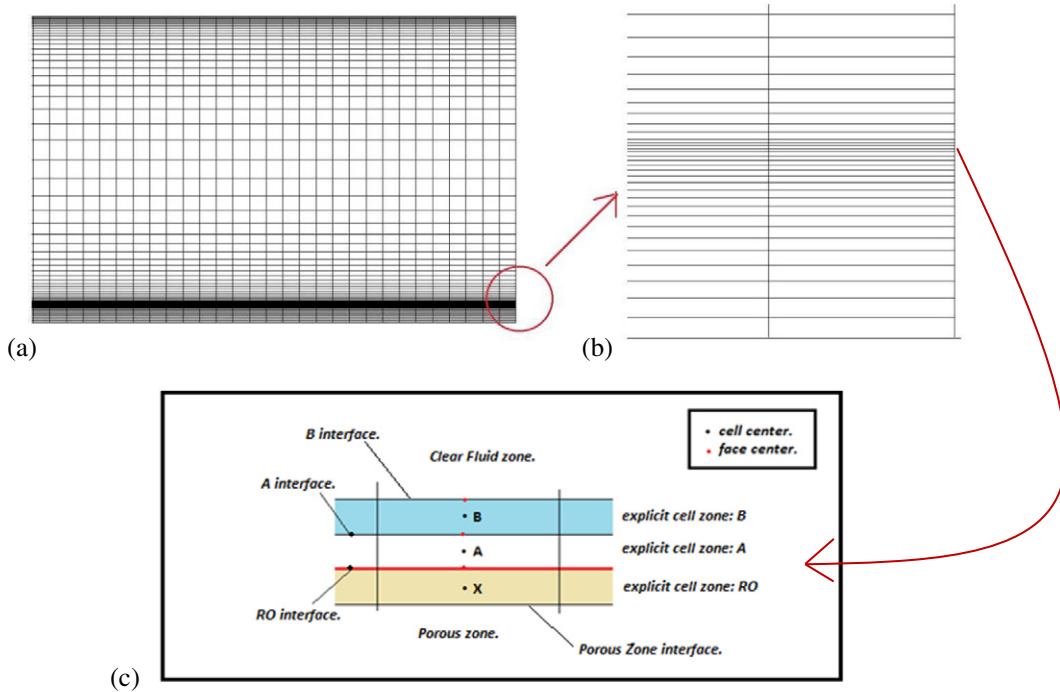


Fig. 3. Computational mesh for simulating flow and transport, (a) of entire domain with non-uniform grid in axial direction, (b) enlarged view near the membrane interface, and (c) illustration of the RO zone modeling.



cell thick were created over this RO zone as shown in Fig. 3c. These two zones were labeled as interface cell zone A and interface cell zone B.

Using first order accurate discretization (Eq. (30)), the boundary condition in Eq. (17) gets modified as,

$$JC_m + D \frac{C_m - C_A}{\Delta z} = JC_p. \quad (32)$$

From Eq. (32) the value of the concentration at the surface of the membrane ( $C_m$ ) is obtained and in terms of rejection coefficient,  $R_c$  it is written as,

$$C_m = \frac{DC_A}{D - JR_c \Delta z}. \quad (33)$$

Similarly using the second order accurate discretized form of slope (Eq. (31)), the concentration at membrane surface is obtained as,

$$C_m = \frac{D(4C_A - C_B)}{3D - 2JR_c \Delta z}. \quad (34)$$

After determining the value of concentration using either Eqs. (33) or (34), it was specified as the concentration on the membrane surface (or RO cell zone). Through a UDF it was implemented as a time varying Dirichlet boundary condition for modeling salt transport in rotor cavity. The same value of concentration was also used to calculate the osmotic pressure. Then permeate out-flux was calculated using the relation given in Eq. (19). The same value of  $J$  is set as the boundary condition in Eq. (12) for simulating fluid flow inside the channel. Furthermore a few UDFs were created to implement the concentration dependent flow and transport parameters such as viscosity, density and diffusivity. To incorporate the zero diffusive solute flux at,  $x = L$  we created another

UDF. The flow, transport processes (Eqs. (21)–(24)) and time varying boundary conditions in Eqs. (14), (17) and (19) are coupled. Hence they must be solved simultaneously. In ANSYS-Fluent the governing flow and transport equations are solved iteratively. Inside each iteration loop of flow and transport solver, the algebraic form of BC. (Eqs. (14), (34) and (19)) are evaluated.

An initial guess for  $C_m$  (in this case equal to feed inlet concentration) is used to evaluate  $\Pi$  in Eq. (20). The value of  $\Pi$  is then used in Eq. (19) to evaluate  $J$ , which is later used to evaluate  $C_m$  in Eq. (34). These values from Eqs. (19) and (34) are used as the flow and transport boundary conditions for next iteration. This iteration continues until residual errors satisfy the convergence criteria. A flow chart is given in Appendix A to illustrate the iterative solution procedure that includes a UDF for evaluation of implicit boundary conditions at the membrane.

### 3.1. Validation of the solution–diffusion RO model

The comparison of the simulated steady state concentration profiles along the depth with the experimental results is presented in Fig. 4 for two different values of Reynolds numbers. It is evident that at both locations from the inlet the simulated profiles are very consistent with the experimentally obtained profiles. As the profiles obtained by 2nd order numerical discretization of boundary condition match better with experimental profiles, Eq. (34) was used for all later simulations.

### 3.2. Grid independence for the rotary system

The fluid flow inside a rotary cavity is quite complex and can attain different regimes depending on the Reynolds number and aspect ratio (see Fig. 2 in [23]). In the present set-up (Fig. 1) the flow was even

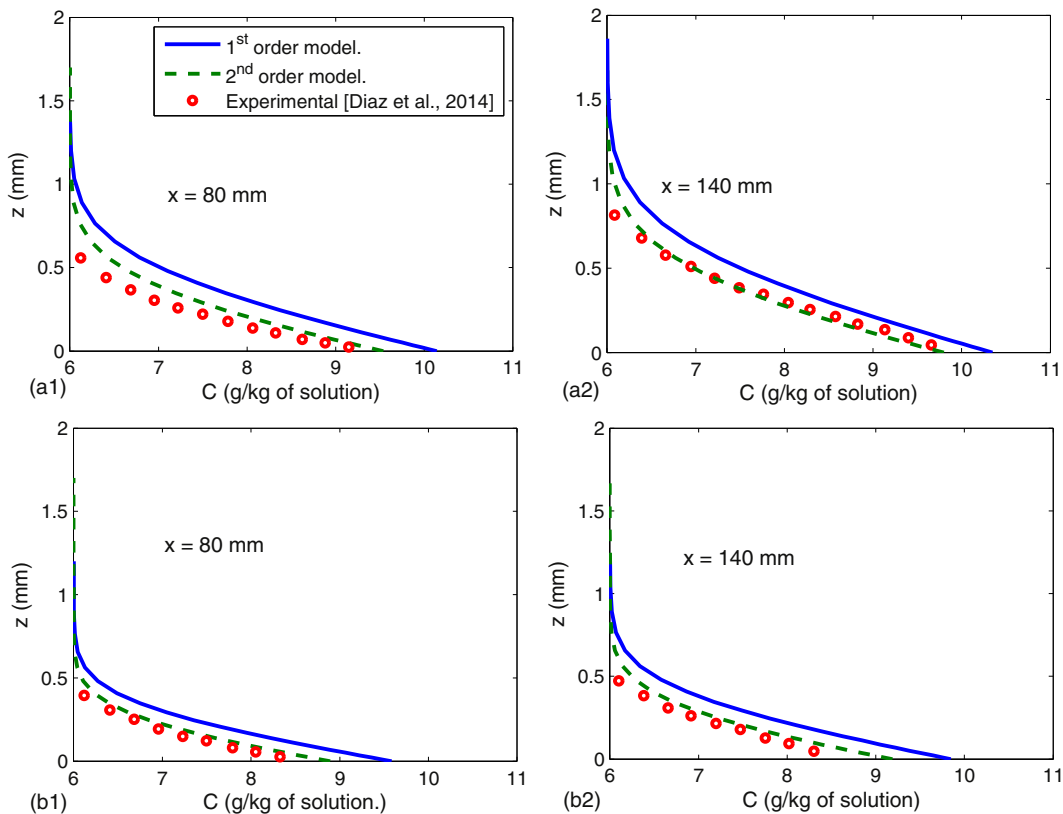
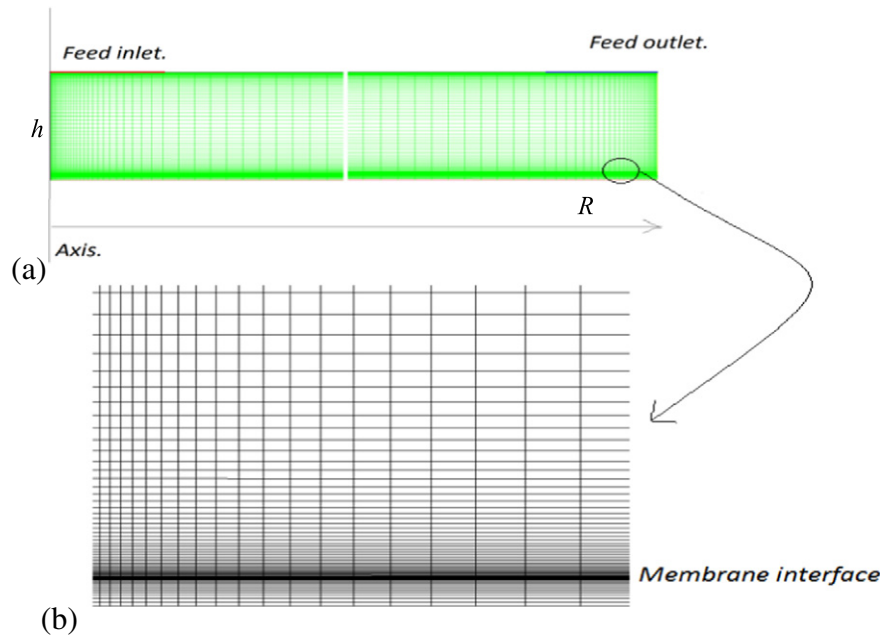


Fig. 4. Comparison of transverse concentration profiles at different locations from the inlet in channel flow system for different values of Reynolds number: (a1, a2)  $Re = 13$  and (b1, b2)  $Re = 38$ .



**Fig. 5.** Computational mesh for simulating flows and transport in rotary system: (a) snipped view of the entire domain and (b) enlarged view at the membrane interface.

more complex due to the presence of feed flow and flux permeating through the membrane. Fig. 5 shows the computational grid used for simulations. The aspect ratio being very small the domain becomes slender and hence a snipped view is presented in Fig. 5a. The enlarged view at the membrane interface represents the fine mesh that is required to capture the concentration gradients.

However, to the best of authors' knowledge, there is no published result to validate the flow field with the boundary conditions in Eqs. (11)–(17) and (19). Poncet et al. [26,27] included feed flow while carrying out the experimental study of flow in a rotary system as shown in Fig. 6. The aspect ratio for their experimental setup was taken as  $G = 0.036$ . They created the flow field with Reynolds numbers

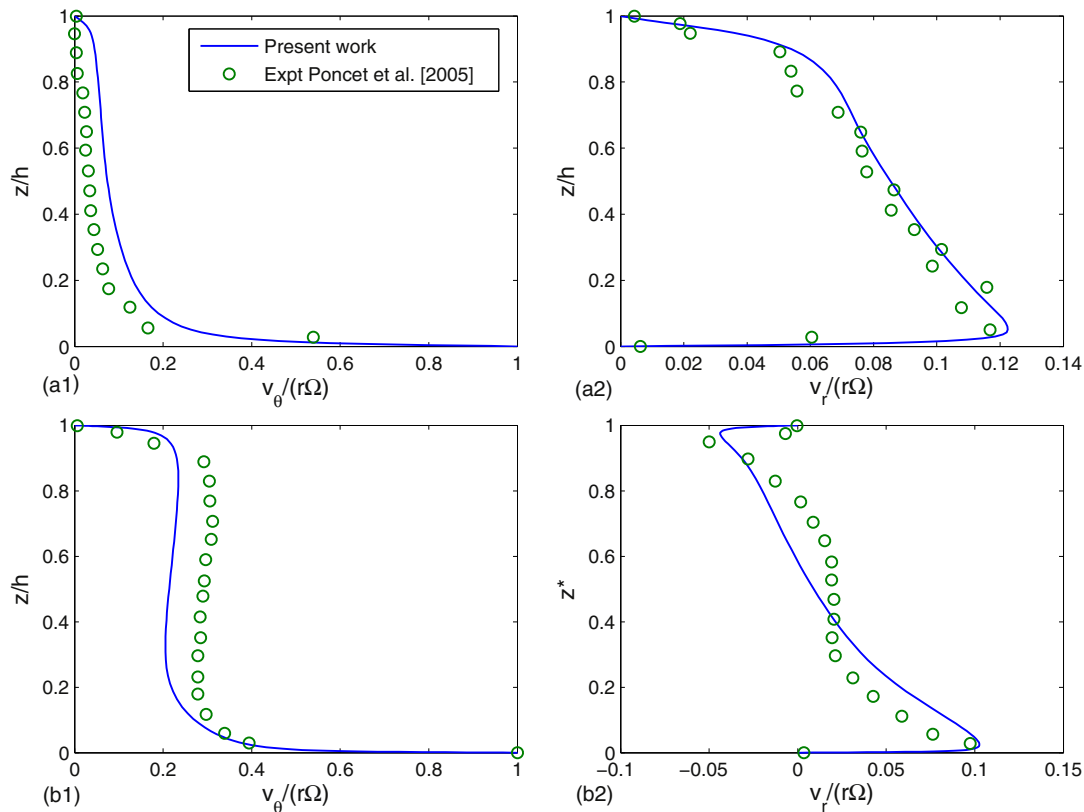


**Fig. 6.** For a rotary system the comparison of swirl and radial velocity components at  $r/R = 0.56$  with experimental results for  $G = 0.036$ ,  $Q^* = 5200$  and different values of Reynolds numbers: (a1, a2)  $Re = 1 \times 10^6$  and, (b1, b2)  $Re = 4.15 \times 10^6$ .

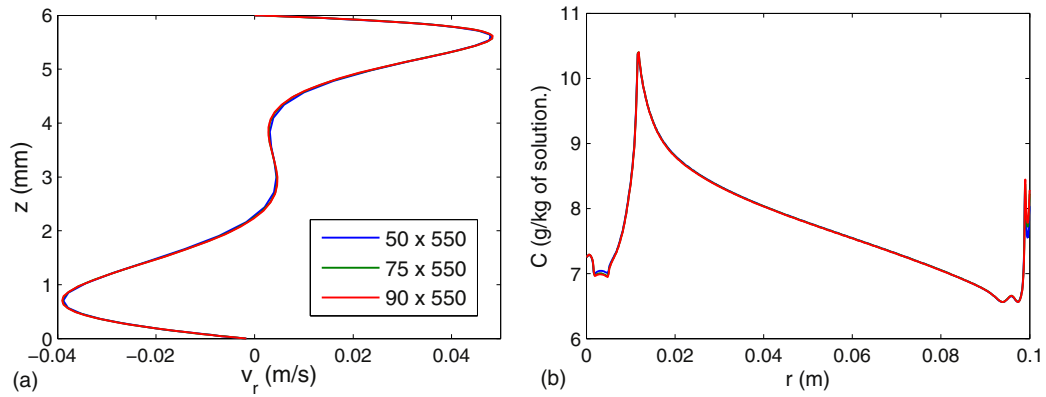


Fig. 7. Comparison of velocity and concentration fields for different grid resolutions: (a) radial velocity components at  $r/R = 0.6$  and (b) radial distribution of solute concentration.

of  $1 \times 10^6$  and  $4.15 \times 10^6$  by rotating the bottom disk and keeping the top disk stationary. From their experimental data the value of dimensionless feed flow rate ( $Q^*$ ) was calculated and it was approximately equal to 5200. Since the Reynolds numbers are very large, based on study by Daily et al. [25] it is expected that the flow is turbulent in nature. So we have simulated the flow using the SST  $k-\omega$  model which is in-built in ANSYS-Fluent V14.5. For both values of Reynolds number, our numerical simulation was verified with their experimental study by comparing the swirl and radial velocity profiles along the depth. Fig. 6 indicates good agreement between the numerical simulation and experimental study for two Reynolds numbers. However the match for lower Reynolds number was better. So it can be expected that for laminar regime our model can simulate the flow very accurately if suitable grid resolution was used.

While modeling concentration polarization the thickness of the RO zone (indicated in Fig. 3c) also significantly affected the accuracy. The computational mesh was kept finer near the membrane interface to capture the large gradients for solute concentration (see Fig. 3b). The grid independence study was performed for the original problem set up as shown in Fig. 1. As a convergence criterion, for all the scaled RMS residuals the tolerances were set to  $10^{-5}$ . The wall shear stress was monitored to check the arrival of hydrodynamic steady state of the system. The solute concentration at  $r = 0.5R$  on the membrane surface was monitored to check the arrival of steady state concentration distribution on the membrane. The unsteady behavior of concentration polarization is discussed in next section. Here the grid independent results are presented for  $Re = 5 \times 10^4$ ,  $Q^* = 10$ , and  $G = 0.06$ . The number of nodes along the radial direction was taken as 550, since we have noted that beyond this number

the results did not improve further while comparing numerical results with experimental results of Poncet et al. [27] even for very large Reynolds number. The number of nodes along the axial direction was varied from 50 to 90. The vertical velocity profiles at  $r = 0.6R$  and concentration on the membrane surface are compared in Fig. 7 for different computational grids. It is apparent from this figure that number of grids in axial direction is sufficient.

Hence further simulations for the parametric study were mostly carried out using a mesh of  $50 \times 550$  nodes. To study the sensitivity of results on the RO zone thickness, it was varied as 4, 8 and 12  $\mu m$ . Fig. 8 shows that the vertical velocity profiles are almost same but the concentration on membrane surface is different near the exit and entry. As the jump in the solute concentration at the exit of domain is minimal, 4  $\mu m$  as the thickness of RO zone was used for simulations.

#### 4. Results and discussion

It is known that shear rate distribution on the membrane surface directly controls the concentration polarization and subsequently the performance of the reverse osmosis filtration system. In this section we present the results of several simulations for different feed flow configurations, angular speed of the rotor, aspect ratio, feed flow magnitude and feed pressure. These results are followed by the discussions pertaining to the correlation between shear rate distribution and concentration polarization.

Considering that the salt concentration inside the rotor cavity would increase with time we performed unsteady simulation of flow and solute transport. The results of unsteady simulation for different Reynolds

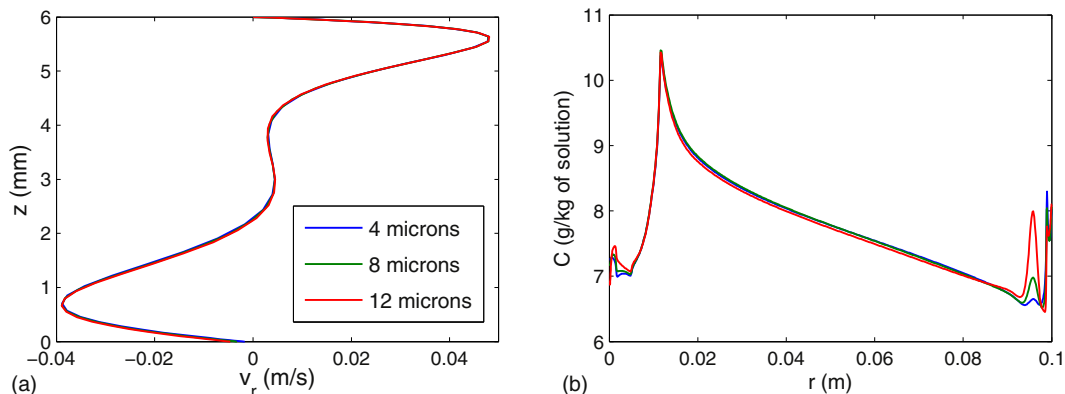
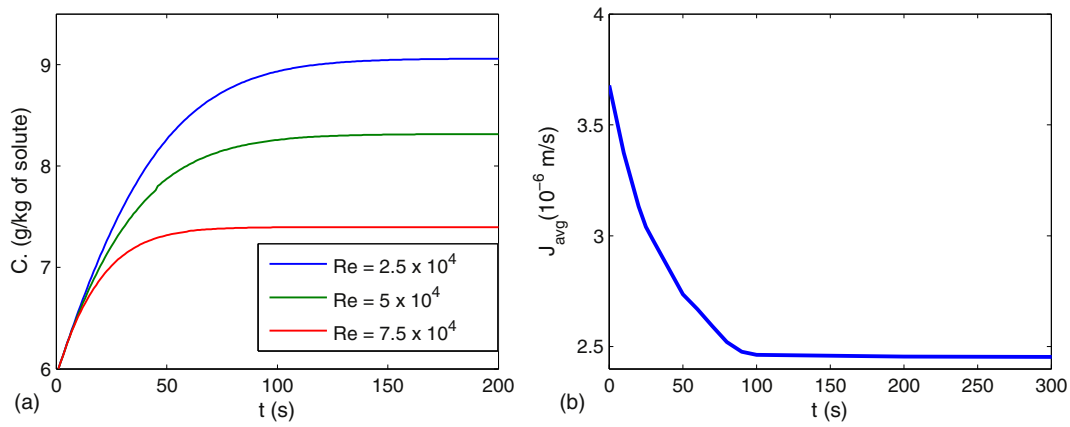


Fig. 8. Comparison of velocity and concentration fields for different RO zone thickness: (a) radial velocity components at  $r/R = 0.6$  and (b) radial distribution of solute concentration.





**Fig. 9.** Results of unsteady simulations to show the arrival of steady state of the system: (a) solute concentration on membrane surface at  $r/R = 0.3$  for different values of Reynolds numbers and (b) average permeate discharge through the membrane for  $Re = 5 \times 10^4$  and  $G = 0.06$ .

numbers are plotted in (Fig. 9). Fig. 9a shows the temporal variation of solute concentration on the membrane surface at  $r = 0.3R$  for different Reynolds numbers. This depicts the salt accumulation on the membrane surface with time. However for all values of Reynolds number the solute concentration reaches a constant value after a short duration. This implies that the salt concentration reaches a steady state. For larger value of  $Re$ , the concentration reaches the steady state faster. Fig. 9b shows the average permeate flux ( $J_{avg}$  in m/s) with time for  $Re = 5 \times 10^4$  and  $G = 0.06$ .

Since the usual operational time of the rotary system is significantly larger than the required time to reach steady state, steady state simulations were performed for the cases simulated further and the parametric study. The steady state, non-dimensional velocity profiles and concentration distribution in axial direction are shown in Fig. 10 for different radial locations. The results shown in Fig. 10 were simulated for  $Re = 5 \times 10^4$ ,  $G = 0.06$ ,  $Q^* = 10$ ,  $p_{feed} = 6$  bar and inlet solute concentration of 6 g/kg of solution. As seen in Fig. 10a and b, the swirl and radial components are representative to a stator rotor cavity system. Fig. 10c

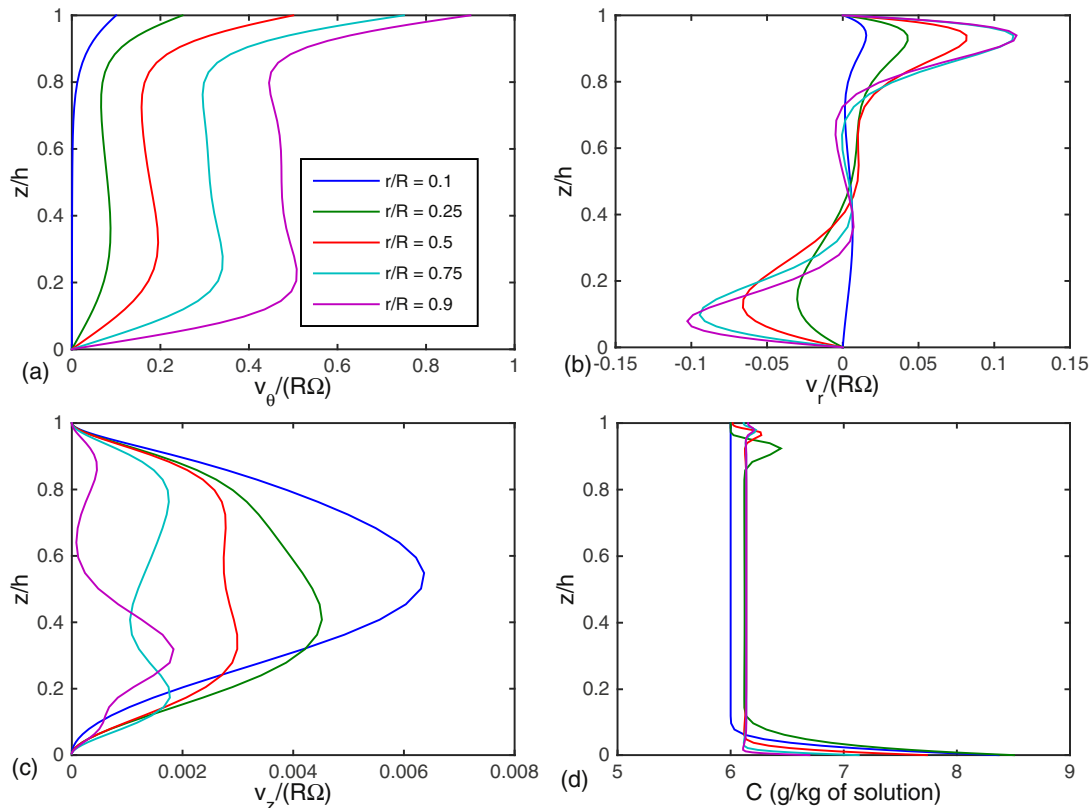


**Fig. 10.** For an outward feed flow system and  $Re = 5 \times 10^4$ ,  $G = 0.06$ ,  $Q^* = 10$  the steady state axial profiles of (a) non-dimensional swirl velocity, (b) non-dimensional radial velocity (c) non-dimensional axial velocity, and (d) solute concentration at different radial locations.

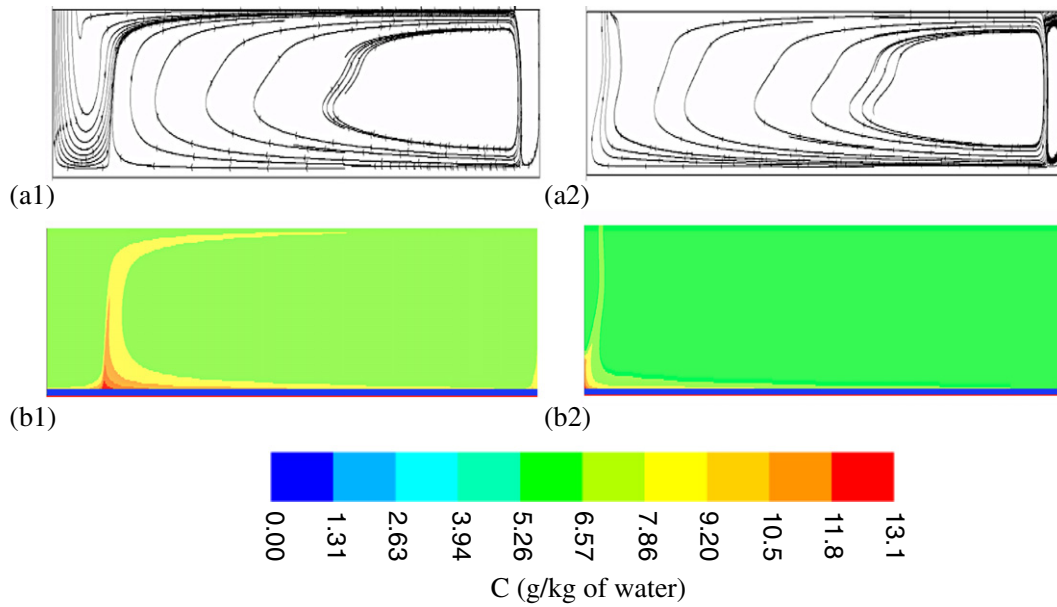


**Fig. 11.** Effect of feed flow configuration on the flow and salt concentration fields: (a) pathlines as projected on the  $r$ - $z$  plane (b) concentration of along the  $r$ - $z$  plane.

shows that the axial velocity component is quite small compared to the swirl and radial components. But its decreasing trend with radius is opposite to that of radial and swirl velocities. In Fig. 10d the distribution of concentration clearly shows the presence of a concentration polarization layer just above the membrane. Due to the circulating flow pattern inside the system a rise of concentration near the rotor is also found. But the magnitude of the peak is much lower than that near the membrane.

#### 4.1. Effect of change in flow configuration

The system configuration can be differentiated based on the feed flow direction depending on the positioning of the inlet and outlet. Fig. 11a illustrates feed flow configuration with the help of pathlines projected onto the  $r$ - $z$  plane, and the corresponding solute concentration distribution within the system. The simulations were performed for  $Re = 5 \times 10^4$ ,  $Q^* = 10$ , and  $G = 0.06$ .

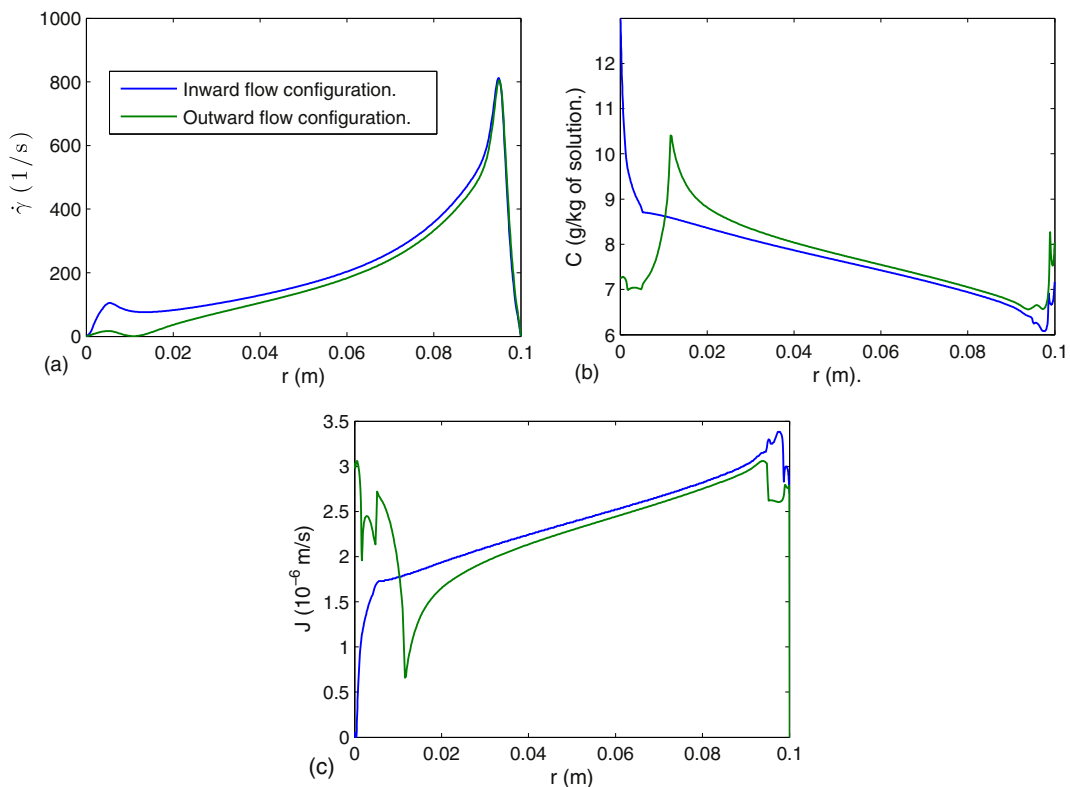


**Fig. 12.** For inward and outward feed flows configuration the radial distribution of (a) total shear rate at the membrane, (b) salt concentration on membrane and (c) permeate flux ( $J$ ) through the membrane.

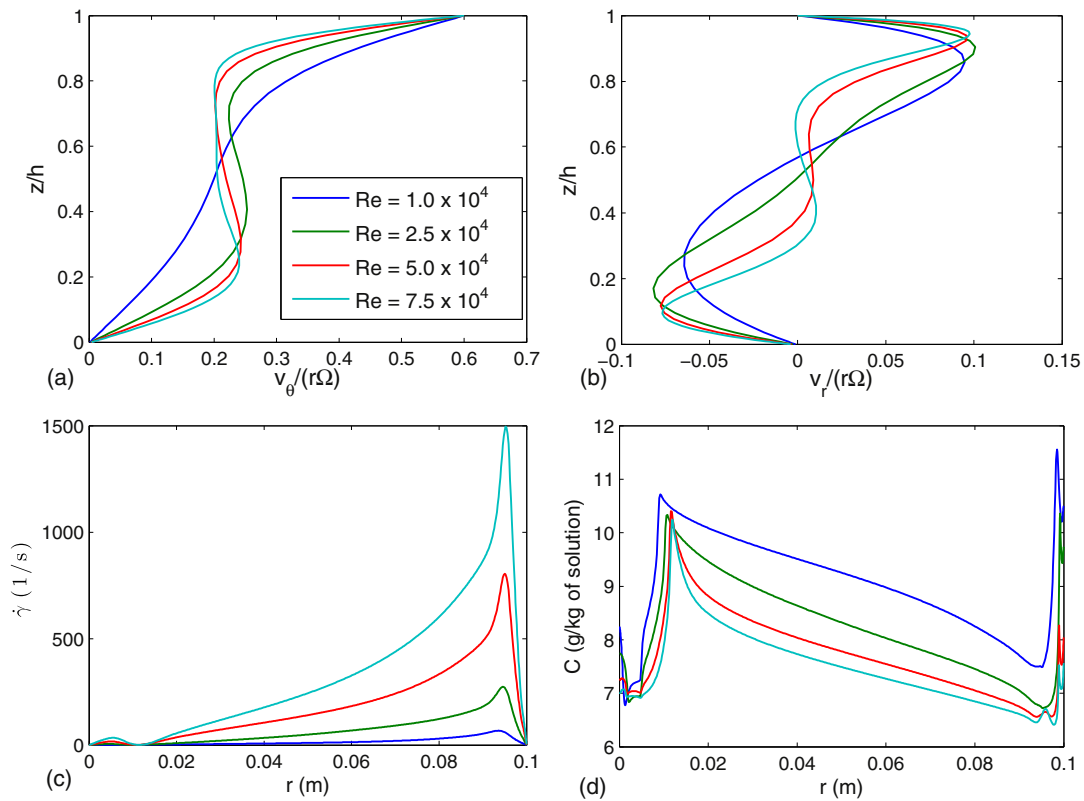


**Fig. 13.** Effects of Reynolds number on (a) non-dimensional swirl velocity profiles, (b) non-dimensional radial velocity profiles at a radial location  $r/R = 0.6$ , (c) radial distribution of shear rate magnitude and (d) solute concentration on the membrane surface.

Inside a closed rotor cavity the flow is three dimensional but axisymmetric. Due to the swirl velocity component fluid particles rotate about the axis of rotation. However due to generation of radial components, fluid particles also travel outward and inward respectively above the stator and below the rotor. When the feed flow is imposed, flow field is altered depending on the direction and magnitude of feed flow discharge.

For the inward and outward feed flow configurations, it is evident from Fig. 11a that the flow patterns near the axis of rotation are quite different. For the outward feed flow case the fluid, which enters downward at the inlet located around the axis travels radially outward from the axis. But the flow over the membrane is in an opposite sense traveling towards the axis. Hence the feed flow gets deflected by this opposite

stream over the membrane, and travels outwards in the vicinity of the rotor as seen from the pathline plot. So there is a point on the membrane surface where the radial component of velocity is zero. But in the case of inward feed flow, since the direction of mean feed flow and the flow on the membrane are in same sense the pathlines turn upward near the axis. The effect of the flow field on the solute concentration distribution is clearly visible in color contour plots in Fig. 11b. Approximately vertical strips of high concentration are observed for both cases. But the locations of the strip are quite different. For outward feed flow case, the strip is located approximately 1 cm away from the axis. On the contrary for the case of inward flow it is located very near the axis.

The radial distribution of shear rate, solute concentration on the surface of membrane and the permeate flux are plotted for both feed flow

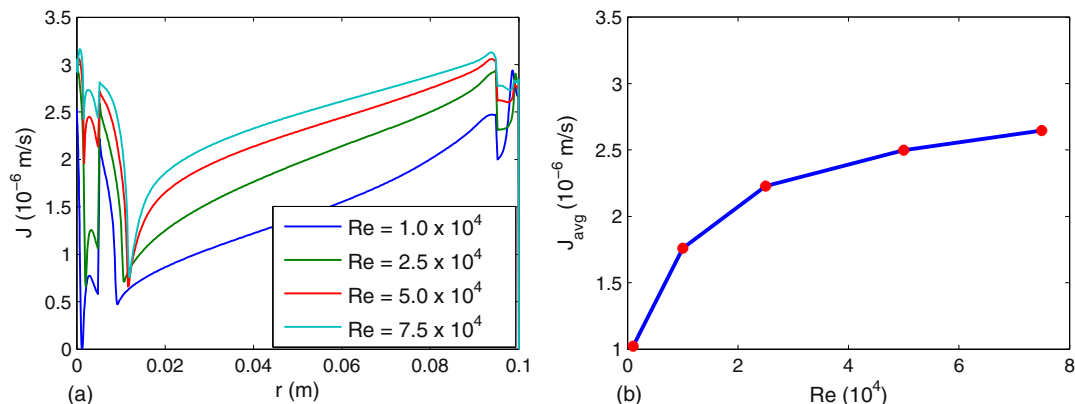


**Fig. 14.** (a) Radial distribution of permeate flux for different values of Reynolds number, and (b) variation of average permeate flux with Reynolds number.

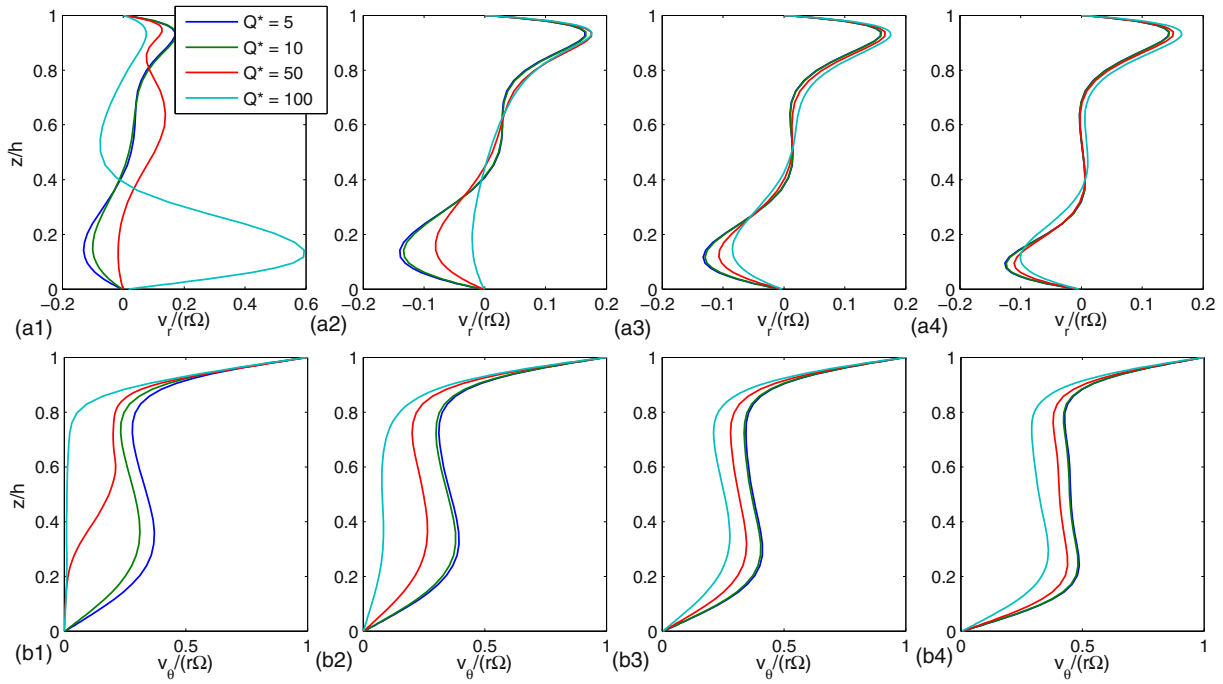


**Fig. 15.** Effect of feed flow ( $Q^*$ ) on the dimensionless (a) radial and (b) swirl velocity profiles at different radial locations from the inlet: (a1, b1)  $r/R = 0.2$ , (a2, b2)  $r/R = 0.4$ , (a3, b3)  $r/R = 0.6$ , and (a4, b4)  $r/R = 0.8$ .

configuration in Fig. 12. Due to the fact that the feed flow merges with the flow over the membrane for inward feed flow case, the shear rate distribution over a large part of the membrane is slightly higher as

compared to the outward flow case. However from Fig. 12a it is noted that the shear rate near the axis of rotation is significantly larger for the inward feed flow case as compared to the outward feed flow case.

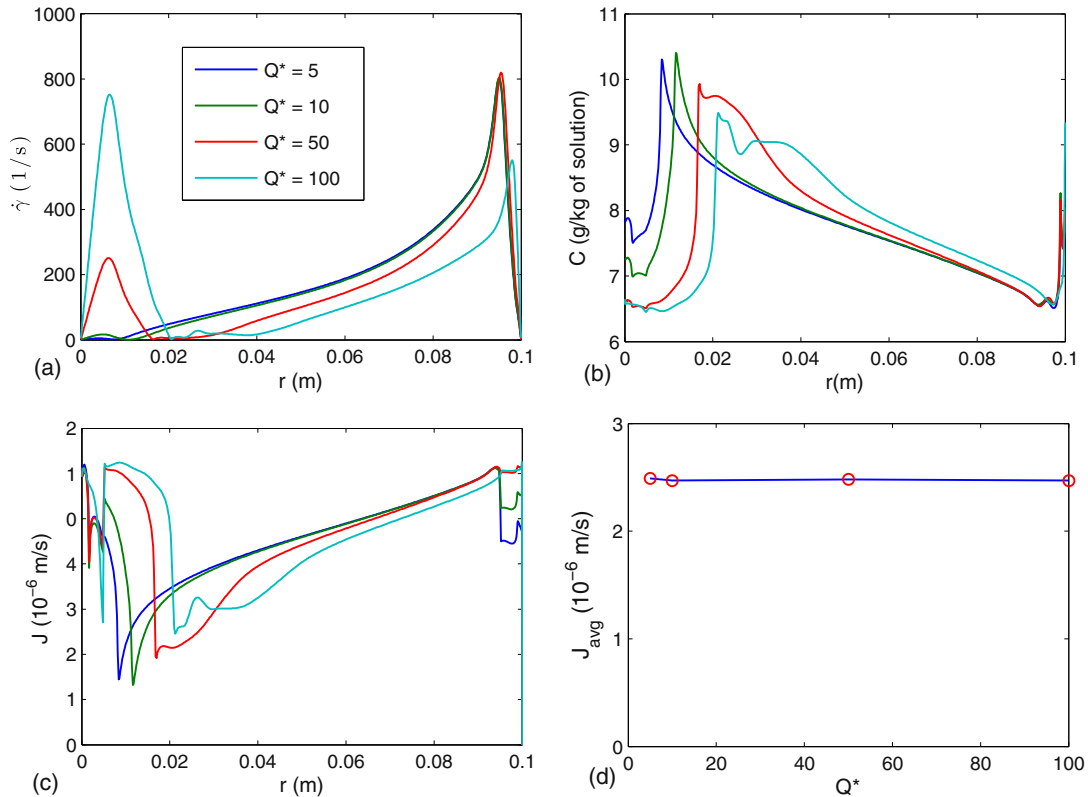


**Fig. 16.** Effects of feed flow on the radial distribution of (a) shear rate magnitude, (b) solute concentration over the membrane surface, and (c) permeate flux. (d) Variation of average permeate flux  $J_{avg}$  with feed flow.

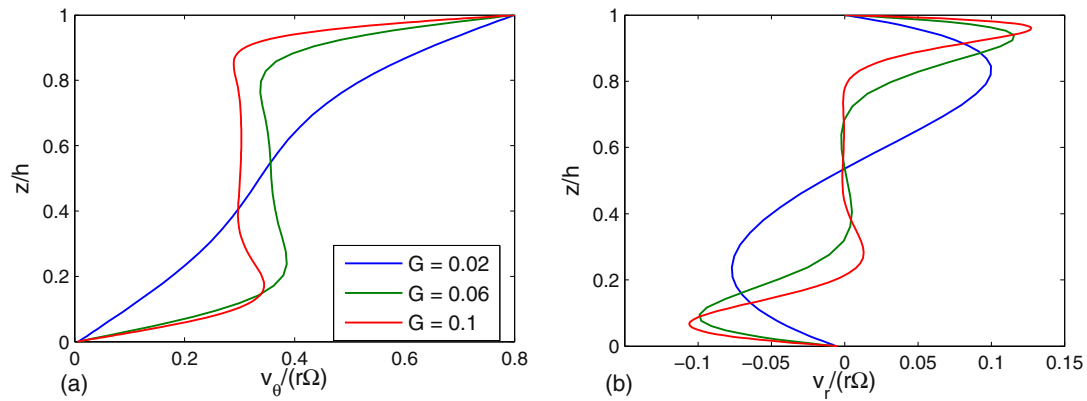


Fig. 17. Effect of aspect ratio on the dimensionless (a) swirl and (b) radial velocity profiles at  $r/R$  0.8.

The shear rate for outward feed flow case is negligible at a location where the radial component of velocity becomes zero. Thus a stagnation zone is present on the membrane surface for outward feed flow case. A quantitative description of concentration polarization on the surface of membrane is presented in Fig. 12b. An inverse relation between shear rate and concentration polarization can easily be realized by comparing the concentration distribution and shear rate distribution respectively in Fig. 12a and b. Except near the exit and entrance, the solute concentration on the membrane surface is slightly smaller for inward feed flow case. For outward feed flow case the concentration is low near the axis as the feed flow entry is located there. However for these cases the salt accumulates at faster rate at the point where the radial velocity is zero (see Fig. 11b) and concentration on the membrane surface

shoots up (Fig. 12b). This point will shift outwards from the axis if the strength of feed flow increases. Hence we can imagine that when the feed flow becomes strong enough in magnitude to dominate over the base flow created by the rotor, the flow over the membrane becomes outward. For the inward flow case, the stagnation zone is located at  $r = 0$  on the membrane. Due to accumulation of solute at  $r = 0$  a peak in the solute concentration is seen in Fig. 12b and a stream of solute starting from  $r = 0$  is seen in Fig. 11b. The mean feed flow direction eventually affects the radial concentration distribution on the membrane surface and permeate flux.

Fig. 12c shows the radial distribution of the permeate flux ( $J$ ) at the membrane outlet surface. The osmotic pressure is a direct function of the solute concentration. So it is expected to follow a similar

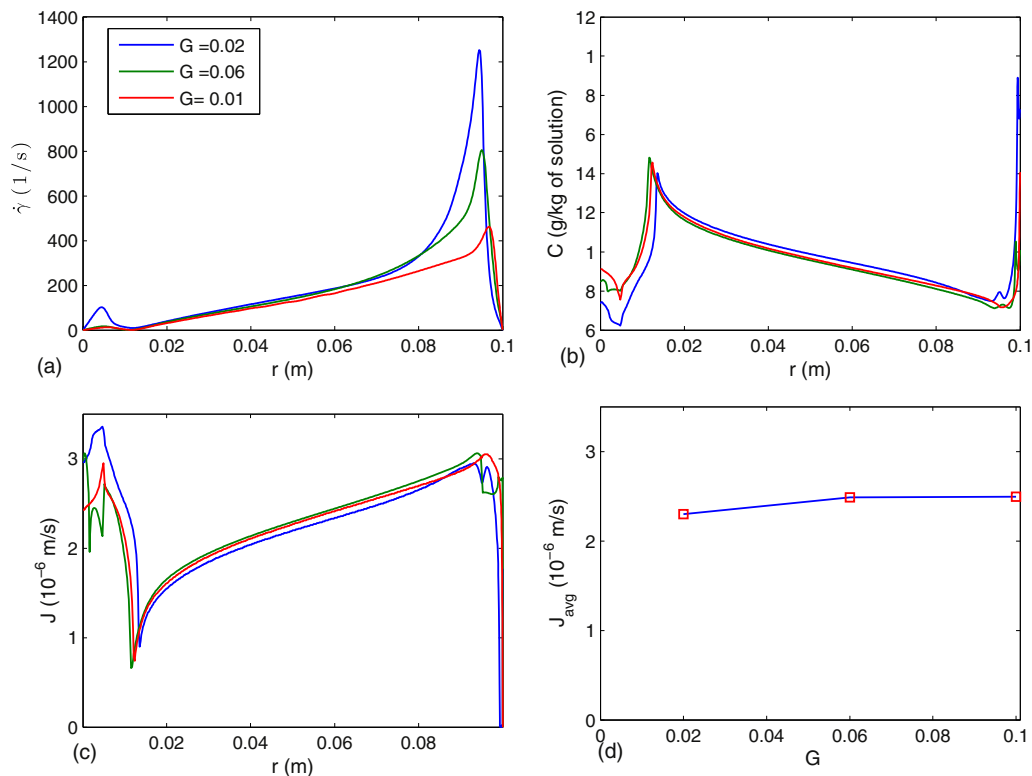


Fig. 18. Effects of aspect ratio on the radial distribution of (a) shear rate magnitude, (b) solute concentration over the membrane surface, and (c) permeate flux. (d) Variation of average permeate flux with aspect ratio.



decreasing trend as radius increases. This leads to increase in net driving pressure across the membrane as radius increases. Hence the permeate flux increases with radius as depicted in Fig. 12c. The average permeate flux ( $J_{avg}$ ) (average volume flow rate per unit membrane surface area) out of the membrane in both of these cases is almost similar, the value for inward flow configuration being  $2.45 \times 10^{-5}$  ( $\text{m}^3/\text{m}^2/\text{s}$ ) and for outward flow configuration being  $2.52 \times 10^{-5}$  ( $\text{m}^3/\text{m}^2/\text{s}$ ).

#### 4.2. Parametric study

Outward feed flow configuration was considered for further simulations to investigate the effect of different parameters such as Reynolds number ( $Re$ ), the non-dimensional feed flow rate ( $Q^*$ ), aspect ratio ( $G$ ), and the feed pressure ( $p_{feed}$ ). For all simulations inlet solute concentration is taken as 6 g/kg of water.

##### 4.2.1. Effect of Reynolds number

In order to study the effect of Reynolds number on the concentration polarization and permeate flux, the angular speed ( $\Omega$ ) of the top rotor has been varied while other parameters held fixed as  $G = 0.06$ ,  $Q^* = 10$  and  $p_{feed} = 6$  bar. The non-dimensional swirl and radial velocity profiles at  $r = 0.6R$  are plotted in Fig. 13.

It is seen that the effect of  $Q^*$  is dominates for low Reynolds number  $Re = 1 \times 10^4$ , but as the Reynolds number increases the rotational effects dominate and we get a velocity profile similar to the stator-rotor cavity flow. Fig. 13b shows the radial velocity profiles gradually change from the merged boundary layer regime to the disjoint boundary layer regime as the angular speed and Reynolds number increases. Fig. 13c shows that for all values of  $Re$  the radial distributions of shear rate on the membrane surface are qualitatively

similar. The shear rate magnitude increases radially with peak values near the exit of the feed solution. The magnitude of shear rate increases with  $Re$ . However the dependence of shear rate magnitude on Reynolds number is non-linear in nature. The radial distribution of solute concentration on the membrane surface is shown in Fig. 13d. The effect of shear rate is quite clearly visible. For larger values of shear rate magnitude, the back diffusion of solute is high and hence salt accumulation is lower.

Fig. 14a shows that the variation of permeate flux ( $J$ ) with  $Re$  is just opposite to that of concentration on the membrane surface. The average permeate flux ( $J_{avg}$ ) that is calculated as the average over the entire membrane surface, is plotted in Fig. 14b. Average permeate output increases with Reynolds number. However reduction in the growth rate of curve representing permeate flux versus Reynolds number implies that rotating the rotor at high speed may not be always be cost effective as it requires more power.

##### 4.2.2. Effect of dimensionless feed flow ( $Q^*$ )

The effect of dimensionless feed flow ( $Q^*$ ) is studied for  $Re = 5 \times 10^4$ ,  $G = 0.06$  and  $p_{feed} = 0.6$  bar. The values for  $Q^*$  are chosen as 5, 10, 50 and 100 such that main characteristics of the base flow in the closed stator-rotor cavity system are retained. Fig. 15 shows the radial and swirl velocity components at different radial locations of  $r = 0.2R, 0.4R, 0.6R$  and  $0.8R$  for different values of  $Q^*$ . It is observed that for  $Q^* = 50, 100$  the flow pattern is quite different from small value of  $Q^*$ . So when the magnitude of  $Q^*$  increases the flow pattern starts deviating significantly from the closed stator-rotor cavity system.

In Fig. 16a the radial distribution of shear rate magnitude are shown. The curves have two peaks. The peak near the outlet (i.e. near  $r = 0.1$  m) is due to higher value of swirl velocity that is created by rotor. The other

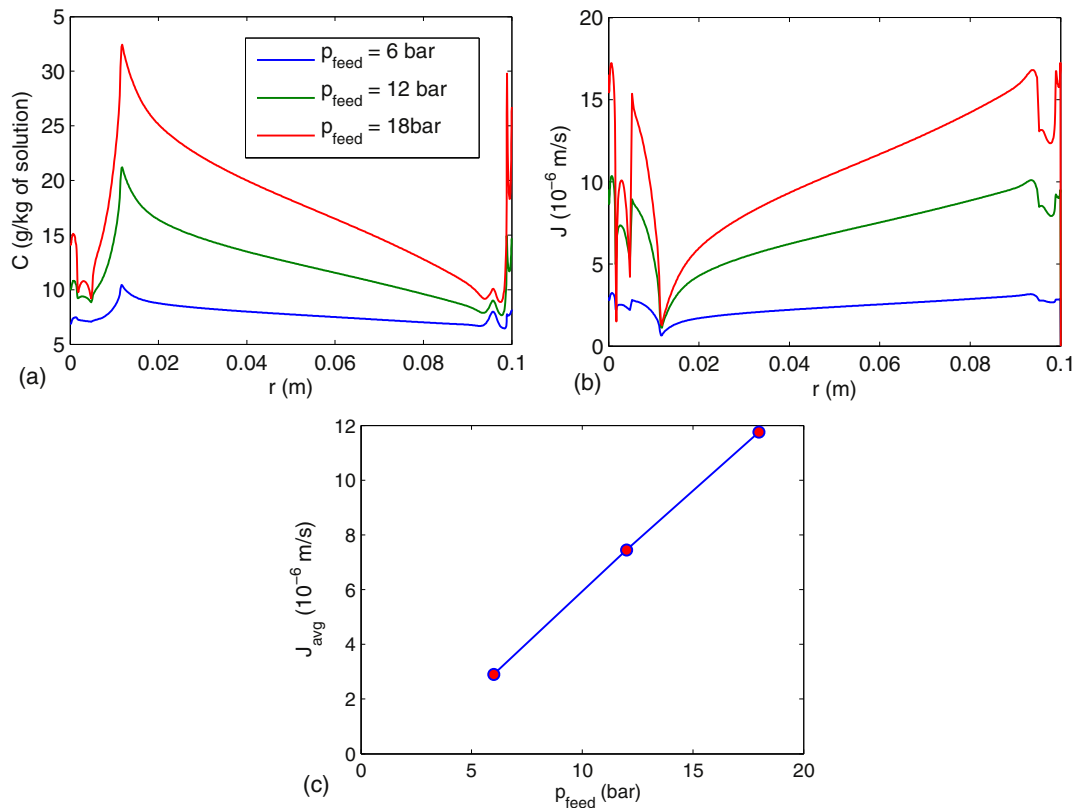


Fig. 19. Effects of feed pressure on the radial distribution of (a) solute concentration over the membrane surface, and (b) permeate flux. (c) Variation of average permeate flux with feed pressure.

peak near inlet (i.e. near  $r = 0.01$  m) is due to higher value of radial velocity of flow as created by the radial configuration of feed flow. As the magnitude of  $Q^*$  increases, the peak near the inlet increases and the stagnation zone (where shear rate is almost zero) shifts away from the axis. However beyond the stagnation zone, the shear rate magnitude decreases with the increase of  $Q^*$ . A notable drop of shear rate near feed flow exit for  $Q^* = 100$  implies that nature of the flow changes. The solute concentration variation with respect to  $Q^*$  is shown in Fig. 16b. The peak of the solute concentration corresponding to the stagnation zone (in Fig. 16b and c) is seen to shift towards the exit of the domain. The concentration in the region between the inlet and exit also increases with  $Q^*$  due to the reduction in shear rates. The radial distributions of permeate flux ( $J$ ) for all values of  $Q^*$  are shown in Fig. 16c. Except at locations very near to the inlet and outlet, the curves showing the distribution concentration and permeate flux are opposite. The erratic behavior of the permeate flux distribution (see Fig. 16c) near the axis (inlet) and at the edge of the disk (outlet) can be accredited to the entrance and the exit effects where the fluid impinges on the membrane to produce such patterns. Even though the radial distributions of permeate flux vary significantly among the cases with different values of  $Q^*$ , Fig. 16d shows that the average permeate flux ( $J_{avg}$ ) is surprisingly uniform.

#### 4.2.3. Effect of aspect ratio ( $G$ )

The simulation parameters used to study the effect of aspect ratio are:  $Re = 5 \times 10^4$ ,  $Q^* = 10$ , and  $p_{feed} = 0.6$  bar. Three different values of aspect ratio ( $G = 0.02, 0.06$  and  $0.1$ ) were considered. The non-dimensional swirl and radial velocity profiles are shown in Fig. 17a and b respectively. For  $G = 0.02$ , the swirl velocity profile is similar to the torsional Couette flow. The corresponding radial velocity plot shows the merged boundary layers at the rotor and the membrane. As  $G$  increases further, we see from the profiles that the boundary layers near the rotor and the membrane are disjoint, and the swirl velocity profile shows a rotating core with a constant non-zero velocity.

For constant angular speed and feed flow discharge, both swirl and radial velocities increase as the aspect ratio decreases. Hence the shear rate magnitude over the entire membrane is larger for smaller value of  $G$ . However Fig. 18a shows that near the inlet and outlet the increase of shear rate is more prominent. Fig. 18b shows that the reduction of salt concentration on the membrane surface is small even though there is significant increase in shear rate distribution.

The effect of the change in aspect ratio on the permeate flux distribution is not pronounced and the curves almost merge and follow a similar trend between the entrance and the exit (Fig. 18c). The entrance and exit effects are observed near the axis and the exit where the variation in flux distributions is not smooth. Fig. 18d shows marginal increase in average permeate flux ( $J_{avg}$ ) for larger aspect ratio.

#### 4.2.4. Effect of feed pressure

The effect of feed pressure on the permeate flux is studied with other parameters kept fixed as  $Re = 5 \times 10^4$ ,  $G = 0.06$ , and  $Q^* = 10$ . Fig. 19 shows the variation of concentration polarization and permeate flux with net driving pressure. The permeate flux increases due to increase of net driving pressure. As the consequence of greater accumulation of salt on the membrane interface the solute concentration increases (see Fig. 19a). The increase in solute concentration on the membrane in turn increases the osmotic pressure. However the development of higher osmotic pressure and increase in permeate flux for higher value of feed pressure reach equilibrium. The nature of solute concentration distribution along the radius is similar for all feed pressure values. This is because the increase in the feed pressure doesn't affect the base flow of the system, even if the permeate flux increases. As seen from Fig. 19c, the increase in the average permeate flux ( $J_{avg}$ ) with feed pressure is significant as compared

to the effect of other parameters discussed previously. The trend seems to be linear.

## 5. Summary and conclusions

Concentration polarization and permeate flux in a roto-dynamic reverse osmosis system were numerically modeled using the commercial code ANSYS-Fluent V14.5, which is a finite volume based computational tool. Several "user defined functions" (UDFs) were written to include the appropriate boundary conditions for modeling reverse osmosis through the membrane and concentration dependent fluid properties (such as density, viscosity, molecular diffusivity, and osmotic pressure). In this study the flow was always set to be in laminar regime. This model was verified against existing experimental results from literature. The implementation of reverse osmosis physics by a separate UDF was tested against the experimental concentration profile in a pressure driven channel reverse osmosis system. Afterwards this computational framework was used to simulate the growth of CP layer in rotary filtration systems and its effects on feed flow hydrodynamics.

The reduction of concentration polarization with the increase of shear rate was evident from the radial distribution of the shear rate and concentration on the membrane surface. The reduction of CP layer with increase in shear rate was also noted while comparing the results of different feed flow configurations. In a roto-dynamic system the shear rate increases as the distance from the axis of rotation increases. However for both radially inward and outward feed flow systems, the plots of shear rate distribution show peaks near the axis of rotation. The plots of concentration polarization on the membrane showed opposite trend, as osmotic pressure is proportional to salt concentration. Except near the inlet and outlet, the permeate flux variations with radius were very similar for radially inward and outward feed flow configurations.

The flow pattern and permeate flux are influenced by the angular speed of the rotor, feed flow rate, aspect ratio and feed pressure as well. As the angular speed increases, the boundary layers on rotor and stator (or membrane) sides get separated. As a result, a thicker rotating fluid core is formed and larger shear rate is generated. Hence the permeate discharge grow with angular speed and so with the Reynolds number (which is based on angular speed of the rotor). However the growth is small for very large values of Reynolds number.

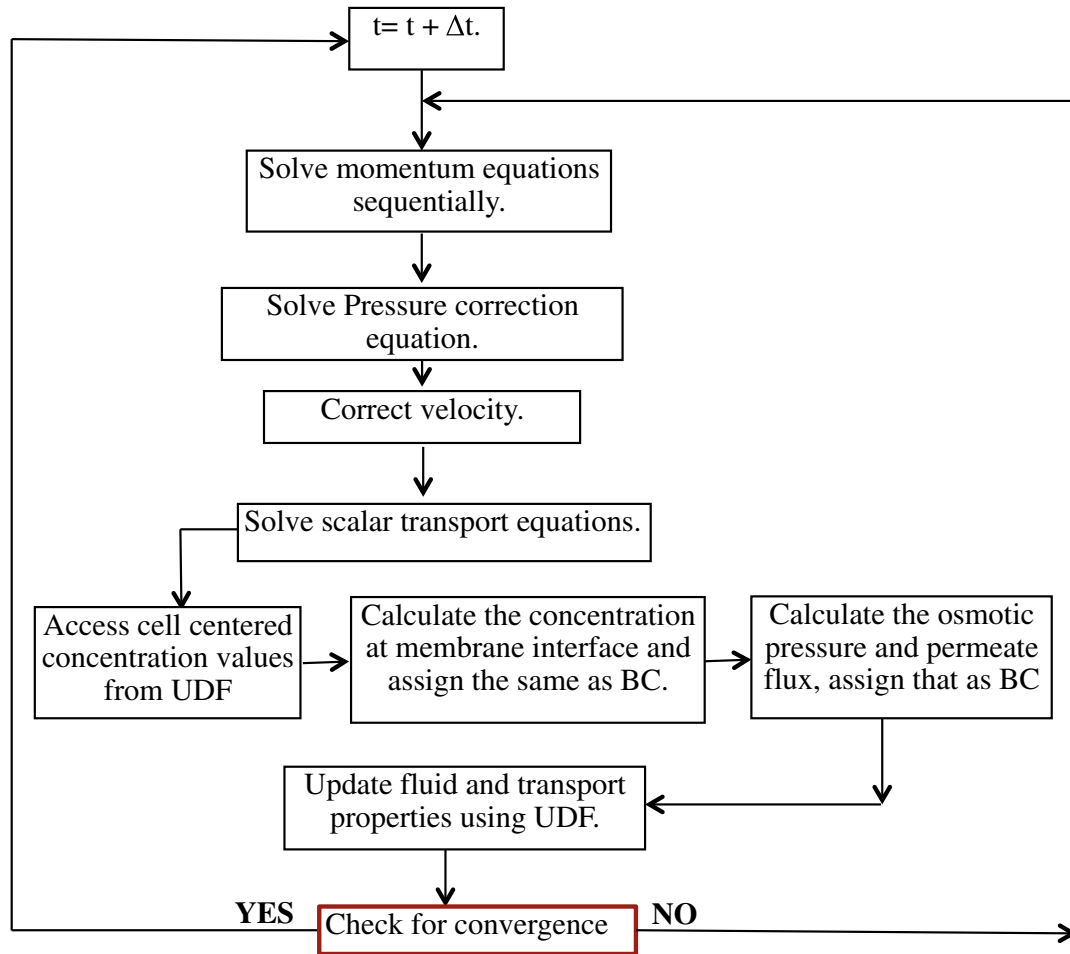
It was observed that magnitude of feed flow rate should be kept small to avoid the radial feed flow superseding the flow characteristics that was generated by the rotating disk. We performed simulations for smaller values of feed flow to understand its effect on average permeate discharge. The distribution of permeate flux with radius was seen to be affected by feed flow rate and peak near the axis was growing. However surprisingly the average permeate flux is nearly constant for a significant range of feed flow rates considered in this study. The aspect ratio also affected the shear rate but the differences in the average permeate discharge for different values of aspect ratio were marginal. Feed pressure was found to be an important parameter since average permeate discharge increased significantly with feed pressure. So in summary we mention that angular speed of the rotor and feed pressure are two important parameters, which can be increased to enhance the permeate discharge.

## Acknowledgments

The authors wish to thank the anonymous reviewers for their constructive comments, which helped to improve the quality of the paper.

## Appendix A

Flow chart illustrating the iterative solution procedure to calculate the permeate flux through membrane:



## References

- [1] J. Johnson, M. Busch, Engineering aspects of reverse osmosis module design, *Desalin. Water Treat.* 15 (1–3) (2010) 236–248.
- [2] A.R. Da Costa, A.G. Fane, D.E. Wiley, Spacer characterization and pressure drop modelling in spacer-filled channels for ultrafiltration, *J. Membr. Sci.* 87 (1994) 79–98.
- [3] F. Li, W. Meindersma, A.B. de Haan, T. Reith, Optimization of commercial net spacers in spiral wound membrane modules, *J. Membr. Sci.* 208 (2002) 289–302.
- [4] F. Li, W. Meindersma, A.B. de Haan, T. Reith, Experimental validation of CFD mass transfer simulations in flat channels with non-woven spacers, *J. Membr. Sci.* 232 (2004) 19–30.
- [5] C.P. Koutsou, S.G. Yiantsios, A.J. Karabelas, Numerical simulation of the flow in plane channel containing a periodic array of cylindrical turbulence promoters, *J. Membr. Sci.* 231 (2004) 81–90.
- [6] C.P. Koutsou, S.G. Yiantsios, A.J. Karabelas, Direct numerical simulation of flow in spacer-filled channels: effect of spacer geometrical characteristics, *J. Membr. Sci.* 291 (2007) 53–69.
- [7] C.P. Koutsou, S.G. Yiantsios, A.J. Karabelas, A numerical and experimental study of mass transfer in spacer-filled channels: effects of spacer geometrical characteristics and Schmidt number, *J. Membr. Sci.* 326 (2009) 234–251.
- [8] Anastasios J. Karabelas, Key Issues for Improving the Design and Operation of Spiral-Wound Membrane Modules in Desalination Plants, *Desalination and Water Treatment*, Taylor and Francis, 2013 1–13.
- [9] M. Kostoglou, A.J. Karabelas, On the fluid mechanics of spiral-wound membrane modules, *Ind. Eng. Chem. Res.* 48 (2009) 10025–10036.
- [10] M. Kostoglou, A.J. Karabelas, Mathematical analysis of the meso-scale flow field in spiral wound membrane modules, *Ind. Eng. Chem. Res.* 50 (2011) 4653–4666.
- [11] Margaritis Kostoglou, Anastasios J. Karabelas, Comprehensive simulation of flat-sheet membrane element performance in steady state desalination, *Desalination* 316 (2013) 91–102.
- [12] K. Bian, K. Yamamoto, Y. Watanabe, The effect of shear rate on controlling the concentration polarization and membrane fouling, *Desalination* 131 (2000) 225–236.
- [13] V. Geraldes, Viriato Semiao, Maria Norberta de Pinho, The effect on mass transfer of momentum and concentration boundary layers at the entrance region of a slit with a nano-filtration membrane wall, *Chem. Eng. Sci.* 57 (2002) 735–774.
- [14] Michel Y. Jaffrin, Dynamic shear-enhanced membrane filtration: a review of rotating disks rotating membranes and vibrating systems, *J. Membr. Sci.* 324 (2008) 7–25.
- [15] Michel Y. Jaffrin, Dynamic filtration with rotating disks, and rotating and vibrating membranes: an update, *Curr. Opin. Chem. Eng.* 1 (2012) 171–177.
- [16] M. Frappart, O. Akoum, L.H. Ding, M.Y. Jaffrin, Treatment of dairy process waters modelled by diluted milk using dynamic nanofiltration with a rotating disk module, *J. Membr. Sci.* 282 (2006) 465–472.
- [17] G.K. Batchelor, Note on a class of solutions of the Navier–Stokes equations representing steady rotationally symmetric flow, *Q. J. Mech. Appl. Math.* 4 (1) (1951) 29–41.
- [18] G.L. Mellor, P.J. Chapple, V.K. Stokes, On the flow between a rotating and a stationary disk, *J. Fluid Mech.* 31 (1) (1968) 95–112.
- [19] K. Stewartson, On the flow between two rotating coaxial disks, *Proc. Camb. Philos. Soc.* 49 (1953) 333–341.
- [20] D. Dijkstra, G.J.F. Van Heijst, The flow between two finite rotating disks enclosed by a cylinder, *J. Fluid Mech.* 128 (1983) 123–154.
- [21] P.J. Zandbergen, D. Dijkstra, von Karman swirling flows, *Annu. Rev. Fluid Mech.* 19 (1987) 465–491.
- [22] J.F. Brady, L. Durlofsky, On rotating disk flow, *J. Fluid Mech.* 175 (1987) 363–394.

- [23] Brian Launder, Sebastien Poncet, Eric Serre, Laminar, transitional, and turbulent flows in rotor–stator cavities, *Annu. Rev. Fluid Mech.* 42 (2010) 229–248.
- [24] Crespo del Arco, E. Serre, P. Bontoux, B.E. Launder, Stability, Transition and Turbulence in Rotating Cavities, *Instability of flows*, WIT press, 2005 (ISBN: 1-85312-785-X, ISSN 1353-808X).
- [25] J.W. Daily, R.E. Nece, Chamber dimension effects on induced flow and frictional resistance of enclosed rotating disks, *ASME J. Basic Eng.* 82 (1960) 217–232.
- [26] Sebastien Poncet, Marie-Pierre Chauve, Patrice Le Galz, Turbulent rotating disk flow with inward through flow, *J. Fluid Mech.* 522 (2005) 253–262.
- [27] Sebastien Poncet, Roland Schiestel, Marie-Pierre Chauve, Centrifugal flow in a rotor–stator cavity, *J. Fluids Eng.* 127 (4) (2005) 784–787.
- [28] Roger Bouzerar, Patrick Paullier, Michel Y. Jaffrin, Concentration of mineral suspensions and industrial effluents using a rotating disk dynamic filtration module, *Desalination* 158 (2003) 79–85.
- [29] Carles Torras, Jordi Pallares, Ricard Garcia-Vallsa, Michel Y. Jaffrin, CFD simulation of a rotating disk flat membrane module, *Desalination* 200 (2006) 453–455.
- [30] C. Torrasa, J. Pallares, R. Garcia-Vallsa, M.Y. Jaffrin, Numerical simulation of the flow in a rotating disk filtration module, *Desalination* 235 (2009) 122–138.
- [31] Ling Li, Po-Ju. Lin, Kuo-Lun Tung, CFD analysis of fluid flow through a spacer-filled disk-type membrane module, *Desalination* 283 (2011) 140–147.
- [32] J.G. Wijmans, R.W. Baker, The solution–diffusion model: a review, *J. Membr. Sci.* 107 (1995) 1–21.
- [33] S. Sablani, M.F.A. Goosena, R. Al-Belushi, M. Wilf, Concentration polarization in ultra-filtration and reverse osmosis: a critical review, *Desalination* 141 (2001) 269–289.
- [34] D.R. Paul, Reformulation of the solution–diffusion theory of reverse osmosis, *J. Membr. Sci.* 241 (2004) 371–386.
- [35] A.L. Ahmad, K.K. Lau, M.Z. Abu Bakar, S.R.Abd. Shukor, Integrated CFD simulation of concentration polarization in narrow membrane channel, *Comput. Chem. Eng.* 29 (2005) 2087–2095.
- [36] S. Wardeh, H.P. Morvan, CFD simulations of flow and concentration polarization in spacer-filled channels for application to water desalination, *Chem. Eng. Res. Des.* 86 (2008) 1107–1116.
- [37] Enrico Díaz-Salcedo, P. García-Algado, M. García-Rodríguez, J. Fernández-Sempere, F. Ruiz-Beviá, Visualization and modeling of the polarization layer in crossflow reverse osmosis in a slit-type channel, *J. Membr. Sci.* 456 (2014) 21–30.
- [38] G. Hoek, Albert S. Kim, Menachem Elimelech, Influence of crossflow membrane filter geometry and shear rate on colloidal fouling in reverse osmosis and nanofiltration separation, *Environ. Eng. Sci.* 19 (6) (2002).

## Abbreviations

CP: concentration polarization  
RO: reverse osmosis

NF: nano-filtration  
CFRO: cross flow reverse osmosis  
UDF: user defined function

## Notations

$R$ : radius, (m)  
 $h$ : gap between the stator and rotor, (m)  
 $\Omega$ : angular speed of the rotor, (rad/s)  
 $Re$ : Reynolds number  
 $r$ : radial co-ordinate  
 $\theta$ : azimuthal co-ordinate  
 $z$ : axial co-ordinate  
 $G$ : aspect ratio  
 $Q$ : feed flow rate, (m<sup>3</sup>/s)  
 $Q^*$ : non-dimensional Feed flow rate  
 $\mu$ : dynamic viscosity, (Pa·s)  
 $\rho$ : density, (kg/m<sup>3</sup>)  
 $\nu$ : kinematic viscosity, (m<sup>2</sup>/s)  
 $K$ : membrane constant, (m/Pa·s)  
 $k$ : permeability of the porous membrane, (m<sup>2</sup>)  
 $h_m$ : thickness of the membrane, (m)  
 $v_\theta$ : swirl velocity, (m/s)  
 $v_r$ : radial velocity, (m/s)  
 $v_z$ : axial velocity, (m/s)  
 $\dot{\gamma}$ : shear rate, (1/s)  
 $p$ : pressure, (Pa)  
 $p_p$ : pressure on the permeate side, (Pa)  
 $p_{atm}$ : atmospheric pressure, (Pa)  
 $C$ : solute concentration, (g/kg of solvent)  
 $D$ : diffusivity of solute, (m<sup>2</sup>/s)  
 $\Pi$ : osmotic pressure, (Bar)  
 $J$ : permeate flux, (m/s)  
 $J_{avg}$ : average permeate flux (m<sup>3</sup>/m<sup>2</sup>·s)  
 $p_{feed}$ : feed pressure, (Bar)  
 $C_p$ : solute concentration at permeate side, (g/kg of solution)  
 $C_m$ : solute concentration at membrane, (g/kg of solution)  
 $C_A$ : solute concentration at a cell center in zone A, (g/kg of solution)  
 $C_B$ : solute concentration at a cell center in zone B, (g/kg of solution)  
 $L$ : length of the CFRO channel (m)  
 $v_x$ : X component of velocity for channel flow, (m/s)  
 $v_y$ : Y component of velocity for channel flow, (m/s)